IEEE Access
Multidisciplinary | Rapid Review | Open Access Journal

Received June 25, 2020, accepted July 15, 2020, date of publication July 20, 2020, date of current version July 31, 2020.

Digital Object Identifier 10.1109/ACCESS.2020.3010584

Multi-Phase-Center Sidelobe Suppression Method for Circular GBSAR Based on Sparse Spectrum

YANPING WANG, (Associate Member, IEEE), QIMING ZHANG, YUN LIN, ZIHENG ZHAO, AND YANG LI

School of Information Science and Technology, North China University of Technology (NCUT), Beijing 100144, China

Corresponding author: Yun Lin (ylin@ncut.edu.cn)

This work was supported in part by the National Key Research and Development Program of China under Grant 2018YFC1505103, in part by the Key International Cooperation projects of the National Natural Science Foundation of China under Grant 61860206013, in part by the Natural Science Foundation of Beijing, China, under Grant 4192019, and in part by the Equipment Pre-Research Foundation under Grant 61404130312.

ABSTRACT Circular ground-based synthetic aperture radar (GBSAR) is a new type of GBSAR with three-dimensional (3D) imaging capability. Its relatively low bandwidth-to-frequency ratio and donut shaped spectrum cause high sidelobes problem, which seriously affects the quality of SAR images. To solve this problem, a multi-phase-center sidelobe suppression method for circular GBSAR based on sparse spectrum is proposed in this paper. This method optimizes the sparse spectrum distribution of multi-phase-center circular GBSAR to suppress the originally high sidelobes. In this paper, the signal model of multi-phase-center circular GBSAR is established, the point spread function (PSF) is derived, and the relationship between the sparse spectrum distribution and the sidelobe level is also analyzed. Moreover, we provide the optimal distribution of the sparse spectrum, thus the optimal distribution of multiple phase centers can be calculated with given imaging geometry, providing the best sidelobe performance. The proposed method is verified via simulation experiments.

INDEX TERMS GBSAR, circular GBSAR, three-dimensional imaging, multi-phase-center, sidelobe suppression, sparse spectrum.

I. INTRODUCTION

In recent years, GBSAR has been used in multiple applications, like landslide monitoring [1], [2], volcano monitoring [3], [4], glacier monitoring [5], [6], open pit monitoring [7], [8], bridge and building monitoring [9]–[12], and so on. However, traditional GBSAR with a straight rail, referred as linear GBSAR, can only acquire two-dimensional (2D) images and can't get the 3D terrain information of monitoring scenes. Because of the "layover" phenomenon, the linear GBSAR is also not suitable for complex terrain. Therefore, the study of GBSAR with 3D imaging capabilities has become a research hotspot in this field.

At present, 3D imaging GBSAR includes multi-baseline linear GBSAR and circular GBSAR. The multi-baseline linear GBSAR forms 2D synthetic aperture by moving the phase center in the azimuth and vertical, to achieve 3D resolution. Its geometry is shown in Figure 1 (a) [13], [14]. Figure 1 (b) is one of its implementations, it uses a horizontal array to scan in the vertical direction. The azimuth aperture is the length of the horizontal array, and the vertical aperture is formed by the movement of the array in the vertical direction [15]. The limitation of the multi-baseline linear GBSAR is its system complexity and time consumption for data acquisition.

The geometry of circular GBSAR is shown in Figure 2 [16]. It forms 2D synthetic aperture through the rotation of the phase center, to achieve 3D imaging [17]. The data acquisition only needs one rotational scan of antenna. Therefore, the system is of low complexity, and the data acquisition is fast.

Currently, circular GBSAR mainly uses a single antenna for data acquisition, we refer it as single-phase-center circular GBSAR [16]. The spectrum of single-phase-center circular GBSAR is donut shaped as shown in Figure 3 (a). Its relatively low bandwidth-to-frequency ratio and donut shaped spectrum cause high sidelobes problem in azimuth and vertical, which seriously affects the imaging quality [18]. In SAR images, the high sidelobes of strong targets will conceal the weak targets nearby, resulting in poor image contrast and low image clarity. Thus, it seriously affects the imaging quality.

The existing sidelobe suppression methods for SAR images mainly include frequency domain windowing method, spectrum reshaping technology, and spatially variant apodization filtering algorithm [19]–[21]. The frequency

The associate editor coordinating the review of this manuscript and approving it for publication was Guolong Cui.

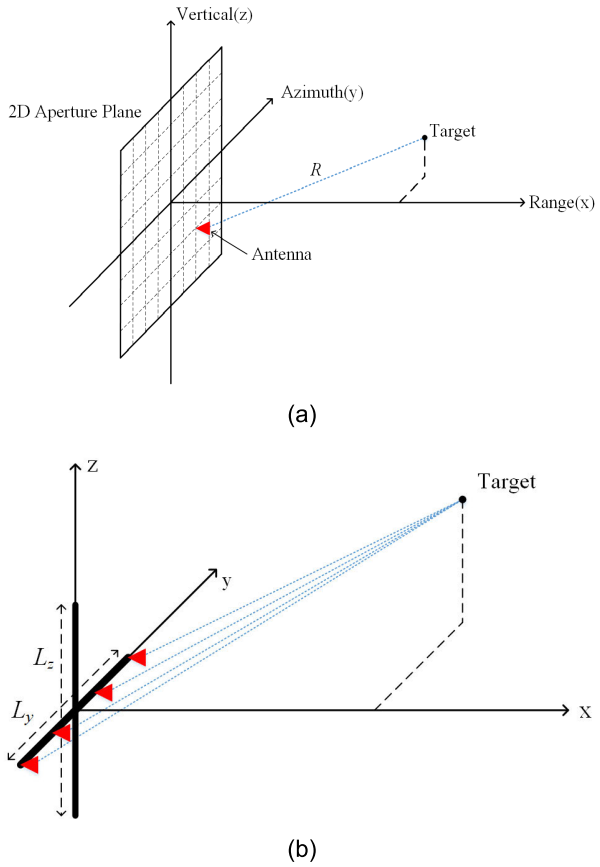

FIGURE 1. Geometry of multi-baseline linear GBSAR (a) imaging mechanism, (b) an implementation.

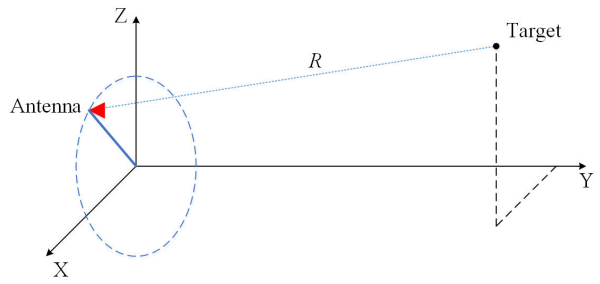

FIGURE 2. Geometry of circular GBSAR.

domain windowing method smooths the edge of spectrum to suppress sidelobes. However, it can't suppress high sidelobes caused by the donut shaped spectrum of circular GBSAR. The spectrum reshaping technology generates the sidelobe direction difference information to realize the separation between the main lobe and the sidelobe. Since the sidelobe of circular GBSAR is omnidirectional, the sidelobe direction can't be changed. Thus, the spectrum deformation technology can't suppress the high sidelobes of circular GBSAR. The spatially variant apodization filtering algorithm finds the minimum amplitude value from a set of raised cosine weighted windowing results to suppress the sidelobes. It also belongs to the windowing method, so it is not applicable

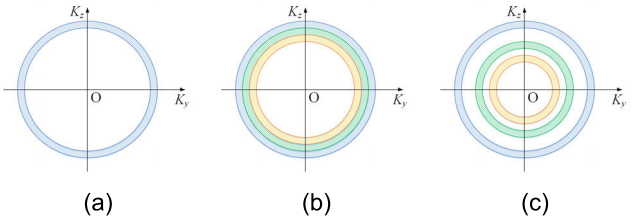

FIGURE 3. The 2D spectrum distribution diagram (a) single-phase-center spectrum, (b) continuously broadened spectrum with multiple phase centers, (c) sparsely optimized spectrum with multiple phase centers.

for suppressing the sidelobes of circular GBSAR. In addition, sparse representation method is another existing sidelobe suppression method. It is a regularization optimization method based on sparse scene, and its point spread function is impulse response [22]–[24]. However, the proposed method suppresses the high sidelobes based on the sparse distribution multiple phase centers.

For the high sidelobe problem of circular GBSAR, a new circular array SAR (CASAR) was proposed in reference [25]. It uses the rotation of an array to form multiple concentric circular apertures, and the final spectrum is still donut shaped but broadened as shown in Figure 3 (b), thus achieving lower sidelobes. However, with a given condition of limited phase center numbers, the length of the array would be very short, and results in weak spectrum broadening effect. Under this condition, the sidelobe can't be effectively suppressed.

In order to effectively solve this problem, a multi-phase-center sidelobe suppression method for circular GBSAR based on sparse spectrum is proposed in this paper. However, the main idea of our method to suppress the sidelobes with limited phase center, is to optimize the sparse distribution of the spectrum. Figure 3 (c) shows the schematic diagram of sparse spectrum distribution. Compared to Figure 3 (b), the spectrum in Figure 3 (c) is not continuous.

The new sidelobe suppression method based on sparse spectrum is proposed to solve the high sidelobe problem of circular GBSAR. It can effectively suppress the high sidelobe, only using a limited phase centers number. When the phase-center number is 3, the proposed method can suppress the maximum sidelobe of circular GBSAR from −7.9dB to −13.8dB, while the maximum sidelobe of traditional linear GBSAR is about −13.2dB. Thus, the proposed method can effectively improve the sidelobe of circular GBSAR. Moreover, the optimal spectrum distribution can be obtained according to the phase change diagram. Meanwhile, the proposed method is available for the whole monitoring scene.

This paper is organized as follows. The geometry and signal model of multi-phase-center circular GBSAR are introduced in Section 2. The spectrum and PSF of circular GBSAR are given in Section 3. Section 4 analyzes the relationship between the spectrum distribution and sidelobes, and proposes an optimization method based on phase change diagram to get the optimal spectrum distribution.

The spatial-variant property of sidelobes is discussed in Section 5, and it verifies that the optimal spectrum distribution works for the whole observation scene. The proposed method is verified by 3D imaging simulations in Section 6. Section 7 discuss the concluding remarks.

II. GEOMETRY AND SIGNAL MODEL

Circular GBSAR forms 2D synthetic aperture by rotating the phase center, so it has resolving capability in azimuth and vertical, and its range resolution is related to the signal bandwidth. Thus, it has 3D resolving capability. This section introduces the geometry and signal model of multi-phase-center circular GBSAR.

A. GEOMETRY

The geometry of multi-phase-center circular GBSAR is shown in Figure 4. N phase centers are sparsely distributed on the rotating arm. They make one rotation around X axis, and form N concentric circular apertures in the YOZ plane. These phase centers observe the target area for the whole aperture.

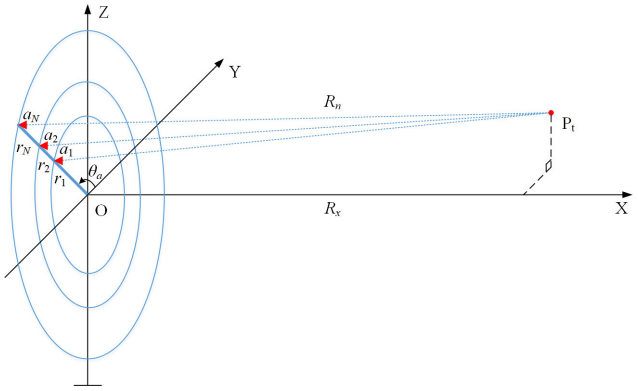

FIGURE 4. Geometry of multi-phase-center circular GBSAR.

In Figure 4, point O is the rotation center of phase centers, $a_1, a_2, \ldots, a_N$ represent phase centers, $r_1, r_2, \ldots, r_N$ are the rotating radius of phase centers, r_N is equal to the length of the rotating arm L, N is the number of phase centers (when $N = 1$, Figure 4 shows the geometry of single-phase-center circular GBSAR), θ_a is the instantaneous rotation angle of phase centers, P_t represents the point target, R_n is the distance between phase center a_n and point target P_t, R_x is the projection length of R_n in the X direction.

According to the position coordinate of phase center a_n and the position coordinates of point target P_t, the distance R_n between phase center a_n and point target P_t can be expressed as

$$R_n = \sqrt{(x_n - x_p)^2 + (y_n - y_p)^2 + (z_n - z_p)^2}, \quad (1)$$

where, x_n, y_n and z_n are the coordinates of a_n, x_p, y_p and z_p are the coordinates of P_t.

To simplify calculation, the coordinate of phase center a_n can be expressed as $(0, r_n \cos\theta_a, r_n \sin\theta_a)$, r_n is the rotating radius of phase center a_n. Therefore, the slant-range from phase center a_n to point P_t can be obtained as follows

$$R_n(r_n, \theta_a) = \sqrt{(x_p)^2 + (r_n \cdot \cos\theta_a - y_p)^2 + (r_n \cdot \sin\theta_a - z_p)^2}. \quad (2)$$

B. SIGNAL MODEL

Step frequency continuous wave (SFCW) signal, frequency modulated continuous wave (FMCW) signal and linear frequency modulation (LFM) signal can all be used as the transmitted signal of multi-phase-center circular GBSAR. In this section, the linear frequency modulation (LFM) signal is used as the transmitted signal, to introduce the signal model.

Generally, range pulse compression is performed in the frequency domain, so the frequency domain form of the preprocessed echo signal can be expressed as

$$S(\theta_a, f) = \sigma \cdot \sum_{n=1}^{N} \mathrm{rect}\left(f / B_r\right) \cdot \exp\left\{-j4\pi (f + f_c) R_n(r_n, \theta_a)/c\right\}, \quad (3)$$

where, $f \in [-B_r/2, B_r/2]$, σ is the scattering coefficient, B_r is the signal bandwidth, f_c is the center frequency, c is light speed. The symbol Φ is the phase in (3).

After performing range pulse compression in the frequency domain and performing Inverse Fourier Transform (IFT), the time domain expression of range compressed signal can be obtained as follows

$$S_{rc}(\theta_a, t) = \sigma \cdot \sum_{n=1}^{N} \mathrm{sinc}\left\{[t - 2R_n(r_n, \theta_a)]/c\right\} \cdot \exp\left\{-j4\pi f_c R_n(r_n, \theta_a)/c\right\}. \quad (4)$$

where, $t \in [-T_r/2, T_r/2]$, T_r is the pulse width of transmitted signal.

Back-projection (BP) algorithm is used to acquire 2D images [26], [27]. Circular GBSAR can achieve 3D space imaging by superimposing 2D images at different range. The 3D imaging process of multi-phase-center circular GBSAR is shown in Figure 5.

Multi-phase-center circular GBSAR performs imaging on any pixel $P(x, y, z)$, to obtain its pixel value $f(x, y, z)$. Its expression is as follows

$$f(x, y, z) = \sum_{n=1}^{N} \int_0^{2\pi} S_{rc}(\theta_a, t) \cdot \exp\left\{j4\pi f_c R_{yz}(r_n, \theta_a)/c\right\} d\theta_a, \quad (5)$$

where, n represents the nth phase center, $R_{yz}(r_n, \theta_a)$ is the distance from phase center a_n to pixel P.

III. SPECTRUM AND POINT SPREAD FUNCTION

This section mainly introduces the spectrum and the point spread function (PSF) of circular GBSAR. The PSF of multi-phase-center circular GBSAR is formed by superimposing

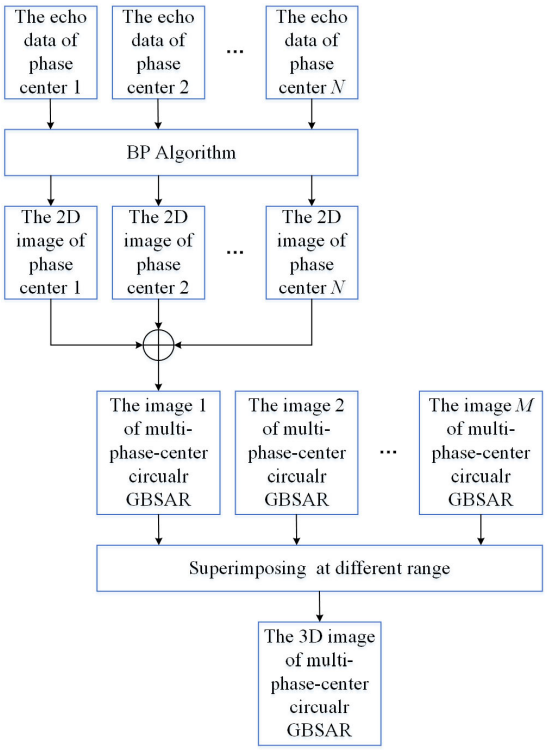

FIGURE 5. The 3D imaging process of multi-phase-center circular GBSAR.

multiple phase centers' PSF. Here, the point target is assumed to be on the rotating axis (X axis).

In order to describe the spectrum of circular GBSAR, the 3D wavenumber domain coordinate system $O_1K_xK_yK_z$ is established. Due to the Fourier characteristic of phase-modulated signal, the instantaneous wave numbers K_y and K_z can be obtained by respectively calculating first-order partial derivatives of y_n and z_n for phase Φ. They can be expressed as

$$K_y = \frac{\partial \Phi}{\partial y_n} = -2K\frac{y_n - y_p}{R_n} \tag{6}$$

$$K_z = \frac{\partial \Phi}{\partial z_n} = -2K\frac{z_n - z_p}{R_n} \tag{7}$$

where, Φ is the phase in (3), its expression is shown in (8). Here, K is defined as wave number, its expression is shown in (9).

$$\Phi = -4\pi\,(f + f_c)\,R_n/c \tag{8}$$

$$K = 2\pi(f + f_c)/c \tag{9}$$

where, $K \in [K_{\min}, K_{\max}]$. The instantaneous wave number in the X direction can be expressed as

$$K_x = -\sqrt{4K^2 - K_y^2 - K_z^2} \tag{10}$$

According to (8)-(10), we can obtain the 3D spectrum of single-phase-center circular GBSAR. Assume the point target P_c located on the X axis, its 3D spectrum support is shown in Figure 6.

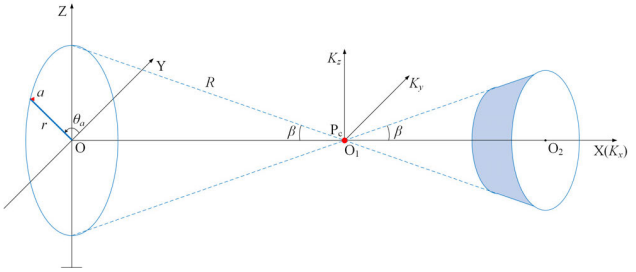

FIGURE 6. The 3D spectrum support of single-phase-center circular GBSAR.

It can be seen from Figure 6 that the spectrum support of single-phase-center circular GBSAR is the outer surface of circular truncated cone. Where, β is the half vertex angle of circular truncated cone. $O_1K_xK_yK_z$ is the wave number domain coordinate system corresponding to the space domain coordinate system $O_1X'Y'Z'$.

The high sidelobes mainly exist in the $O_1Y'Z'$ plane, so we only project the 3D spectrum support of single-phase-center circular GBSAR on the $O_1K_yK_z$ plane. The 2D spectrum support of single-phase-center circular GBSAR in the $O_1K_yK_z$ plane is shown in Figure 7.

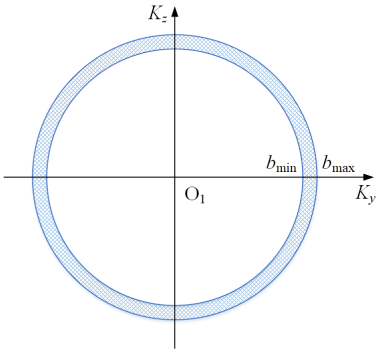

FIGURE 7. The 2D spectrum support of single-phase-center circular GBSAR in $O_1K_yK_z$ plane.

In Figure 7, the outer radius of the 2D spectrum support in the $O_1K_yK_z$ plane is represented as $b_{\max}$, and its inner radius is represented as $b_{\min}$. Their expressions are as follows

$$\begin{cases} b_{\min} = K_{\min} \cdot \sin\beta \\ b_{\max} = K_{\max} \cdot \sin\beta \end{cases} \tag{11}$$

where, the half vertex angle $\beta = \arctan(r/x_c)$, r is the rotating radius of phase center a, x_c is the abscissa of point target P_c.

The PSF is the IFT of the spectrum. The PSF in range is a sinc function, and its expression can be referred to reference [28]. The PSF in the $O_1Y'Z'$ plane is a Bessel function, and it is circular symmetric [28]. It can be expressed as

$$g_{cyz}(\rho) \approx \begin{cases} J_0(b_{\max}\rho) & for\ b_{\min} = b_{\max} \\ \dfrac{2\left[b_{\max}J_1(b_{\max}\rho) - b_{\min}J_1(b_{\min}\rho)\right]}{\rho\left(b_{\max}^2 - b_{\min}^2\right)} & otherwise \end{cases} \tag{12}$$

where, $\rho = \sqrt{(y'^2 + z'^2)}$, $J_0(\cdot)$ is the first kind of zero-order Bessel function, $J_1(\cdot)$ is the first kind of first-order Bessel function, and $b_{\min} = b_{\max}$ indicates that the transmitted signal is single-frequency signal.

Define the ratio α_a to represent the bandwidth-to-frequency ratio of spectrum, and its expression is as follows

$$\alpha_a = (b_{\max} - b_{\min}) \big/ b_{\max} = (K_{\max} - K_{\min}) \big/ K_{\max} \quad (13)$$

where, $\alpha_a \in [0, 1]$. Then $b_{\min}$ can be represented by $b_{\max}$ and α_a, and its expression is as follows

$$b_{\min} = (1 - \alpha_a)\, b_{\max} \quad (14)$$

From (12) and (14), it can be known that the PSF of single-phase-center circular GBSAR is determined by $b_{\max}$ and $b_{\min}$, while its sidelobe is determined by the ratio α_a.

The parameters that affect the 3D imaging performance include center frequency and bandwidth-to-frequency ratio. The 3D imaging performance is reflected in resolution and sidelobes. The signal bandwidth affects range resolution, and the maximum frequency affects azimuth resolution. The bandwidth-to-frequency ratio affects the sidelobes of single-phase-center circular GBSAR. The phase center number and distribution affect the sidelobes of multi-phase-center circular GBSAR.

From Figure 6, we can derive the resolution expression in X direction, and it is as follows

$$\delta_x = c \big/ (2B_r \cos\beta) \quad (15)$$

For circular GBSAR, β is quite small. Thus, the resolution expression in X direction is mainly related to the signal bandwidth B_r.

From Figure 7, we can derive the resolution expression of the $O_1Y'Z'$ plane. From (12), we can know that the PSF in the $O_1Y'Z'$ plane is circular symmetric, so the resolution expression in Y direction is same as that in Z direction. Their expression are as follows

$$\delta_y = \delta_z = \alpha_\Delta(\alpha_a) \cdot \pi \big/ 2b_{\max} = \alpha_\Delta(\alpha_a) \cdot c \big/ (4f_{\max} \cdot \sin\beta) \quad (16)$$

where, the factor α_Δ is related to α_a, and its value range is [0.765, 1.22]. β is determined by the rotating radius r and the target range x_c. Thus, when x_c is given, the resolution of the $O_1Y'Z'$ plane is related to the rotating radius.

For multi-phase-center circular GBSAR, the 3D spectrum support is shown in Figure 8. It is the N outer surfaces of circular truncated cone with different radius.

In Figure 8, $\beta_1, \beta_2, \ldots, \beta_N$ are the half-apex angle of phase center $a_1, a_2, \ldots, a_N$. By projecting the 3D spectrum support of multi-phase-center circular GBSAR into the $O_1K_yK_z$ plane, the 2D spectrum support in this plane can be obtained. It is shown in Figure 9.

It can be seen from Figure 9, the 2D spectrum support of multi-phase-center circular GBSAR in the $O_1K_yK_z$ plane is N concentric circular rings. The outer and inner radius of these rings are denoted by $b_{n\max}$ and $b_{n\min}$. The outer ring radius

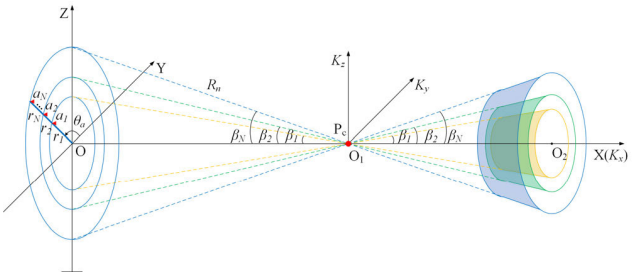

FIGURE 8. The 3D spectrum support of multi-phase-center circular GBSAR.

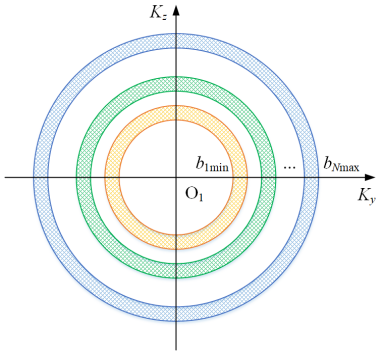

FIGURE 9. The 2D spectrum support of multi-phase-center circular GBSAR in $O_1K_yK_z$ plane.

and inner ring radius are represented by $b_{n\max}$ and $b_{n\min}$. Their expressions are as follows

$$\begin{cases} b_{n\max} = b_{N\max} \cdot \sin\beta_n \big/ \sin\beta_N \\ b_{n\min} = (1 - \alpha_a)\, b_{n\max} \end{cases} \quad (17)$$

where, $b_{N\max}$ is the outer ring radius of Nth phase center. β_n is the half-apex angle of phase center a_n, it can be expressed as

$$\beta_n = \arctan\left(r_n \big/ x_c\right) \quad (18)$$

where, r_n is the rotation radius of phase center a_n.

It can be known from Figure 8 and Figure 9 that the spectrum of multi-phase-center circular GBSAR is formed by superimposing the spectrum of N phase centers. Therefore, the PSF of multi-phase-center circular GBSAR can be expressed by summation of N phase centers' PSF. The PSF in the $O_1Y'Z'$ plane is as follows

$$g_{mcyz}(\rho) \approx \begin{cases} \sum_{n=1}^{N} J_0(b_{n\max}\rho) & for\ b_{n\max} = b_{n\min} \\ \left\{ \sum_{n=1}^{N} \left[b_{n\max} J_1(b_{n\max}\rho) - b_{n\min} J_1(b_{n\min}\rho) \right] \right\} \cdot \dfrac{2}{\rho \sum_{n=1}^{N} \left(b_{n\max}^2 - b_{n\min}^2 \right)} & otherwise \end{cases} \quad (19)$$

It can be known from (19) that the PSF of multi-phase-center circular GBSAR in the $O_1Y'Z'$ plane is related to the

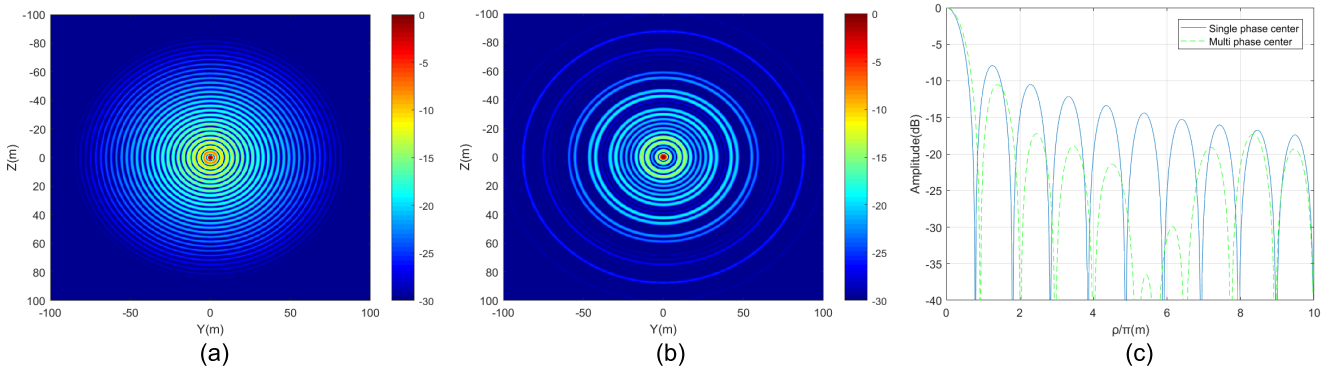

FIGURE 10. The point spread function of circular GBSAR (a) single-phase-center circular GBSAR with higher sidelobe, (b) multi-phase-center circular GBSAR with lower sidelobe, (c) the 1D point spread function in $O_1Y'Z'$ plane.

inner ring radius $b_{n\min}$ and the outer ring radius $b_{n\max}$ of 2D spectrum. Moreover, the sidelobe of multi-phase-center circular GBSAR is determined by the ratio α_a and the spectrum distribution $b_{n\max}/b_{N\max}$.

Equations (16) shows that the resolution of single-phase-center circular GBSAR in the $O_1Y'Z'$ plane is related to the maximum wavenumber $b_{\max}$. Thus, the resolution of multi-phase-center circular GBSAR in the $O_1Y'Z'$ plane is almost the same as that of single-phase-center circular GBSAR, when $b_{N\max}$ is equal to $b_{\max}$.

Figure 10(a) and (b) compares the PSF between single-phase-center circular GBSAR and multi-phase-center circular GBSAR in the $O_1Y'Z'$ plane. In order to show the sidelobe difference, here the maximum outer ring radius of multi-phase-center circular GBSAR $b_{N\max}$ is equal to the outer ring radius of single-phase-center circular GBSAR $b_{\max}$, α_a is same for two models, and the distribution $b_{n\max}/b_{N\max}$ is randomly selected. From (12) and (19), we can know that the PSF in the $O_1Y'Z'$ plane is circular symmetric. Therefore, only the PSF of circular GBSAR in the radial direction is shown in Figure 10(c). Figure 10 shows that the sidelobe of multi-phase-center circular GBSAR in the $O_1Y'Z'$ plane is lower than that of single-phase-center circular GBSAR.

In summary, the PSF of multi-phase-center circular GBSAR is the superimposition of N phase centers' PSF, so its PSF is related to the phase center distribution. By comparing the PSF of single-phase-center circular GBSAR with that of multi-phase-center circular GBSAR, it can be found that the sidelobe of multi-phase-centers circular GBSAR in the $O_1Y'Z'$ plane is lower than that of single-phase-center circular GBSAR.

IV. SIDELOBE SUPPRESSION METHOD BASED ON SPARSE SPECTRUM

The analysis in Section 3 shows that the point spread function (PSF) of circular GBSAR in the $O_1Y'Z'$ plane is Bessel function and it has the high sidelobe problem, while the circular GBSAR with multiple phase center can suppress the sidelobe of the PSF in this plane. In order to find the lowest sidelobe, this section will analyze the relationship between the sidelobe of the PSF in the $O_1Y'Z'$ plane and the sparse spectrum distribution, and use the phase change diagram to find the optimal spectrum distribution under the condition of given phase center number and given bandwidth-to-frequency ratio. Section 4.1 analyzes the relationship between the bandwidth-to-frequency ratio and the sidelobe of single-phase-center circular GBSAR. Under the condition of a given bandwidth-to-frequency ratio, Section 4.2 analyzes how the spectrum distribution of multi-phase-center circular GBSAR affects the sidelobe. Section 4.3 proposes an optimization method based on phase change diagram to get the optimal spectrum distribution for the lowest sidelobe.

A. SIDELOBE OF SINGLE-PHASE-CENTER CIRCULAR GBSAR

From (12) and (14), the point spread function of single-phase-center circular GBSAR is related to the bandwidth-to-frequency ratio α_a and the maximum wavenumber in the $O_1K_yK_z$ plane $b_{\max}$. In order to analyze the influence of bandwidth-to-frequency ratio on the sidelobe, the PSF of single-phase-center circular GBSAR with the same $b_{\max}$ and different α_a is shown in Figure 11.

It can be seen from Figure 11 that when the ratio α_a is 0, 1/2, and 1, the bandwidth is 0, $b_{\max}/2$, and $b_{\max}$, respectively.

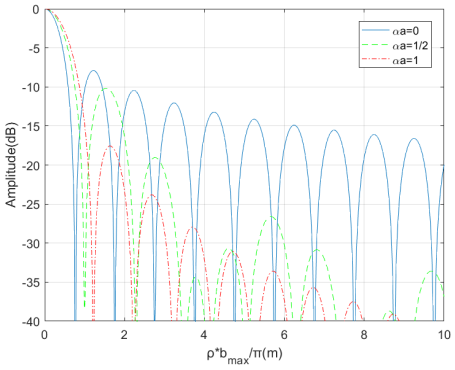

FIGURE 11. The point spread function of single-phase-center circular GBSAR with different α_a.

The sidelobe of the PSF with different ratio is −7.9dB, −10.16dB and −17.57dB. Obviously, the bandwidth-to-frequency ratio significantly influences the sidelobe of single-phase-center circular GBSAR.

Figure 12 shows the peak sidelobe ratio (PSLR) curve with respect to the bandwidth-to-frequency ratio. It can be seen that the larger α_a, the less the unknown region inside the ring-shaped spectrum, the lower sidelobe. In order to get an ideal PSLR, we need to increase the bandwidth-to-frequency ratio α_a as much as possible. However, compared with spectrum bandwidth, the working frequency of radar is quite large in GBSAR applications. Therefore, it is difficult to increase the bandwidth-to-frequency ratio α_a for an acceptable PSLR.

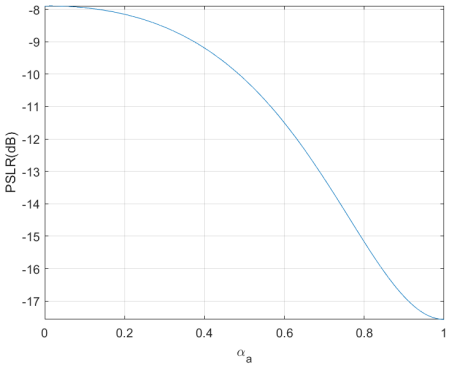

FIGURE 12. α_a – peak sidelobe ratio curve.

B. SIDELOBE OF MULTI-PHASE-CENTER CIRCULAR GBSAR

Multi-phase-center circular GBSAR provides extra spectrum information to the originally unknown region inside the ring-shaped spectrum by superimposing the spectrum of multiple phase centers, to achieve sidelobe suppression. In order to analyze the sidelobe of different spectrum distribution, this section discusses the relationship between different spectrum distribution and the sidelobe under the condition of given phase centers number and given bandwidth-to-frequency ratio.

The spectrum of multi-phase-center circular GBSAR in the $O_1K_yK_z$ plane is a set of concentric rings as shown in Figure 10 (a). Under the conditions of $N = 3$ and $\alpha_a = 0.05$, the sidelobes of continuous distribution, uniformly sparse distribution, and randomly sparse distribution are compared. And they have the same outer ring radius $b_{3\max}$. Figure 13 shows the three typical spectrum distributions in the $O_1K_yK_z$ plane.

Figure 14 shows the point spread function of single-phase-center circular GBSAR and multi-phase-center circular GBSAR with typical spectrum distributions.

It can be seen from Figure 14 that under the condition of a given bandwidth-to-frequency ratio, different spectrum distributions have different effects on sidelobe suppression. The 3D imaging performance of single-phase-center circular GBSAR and multi-phase-center circular GBSAR with

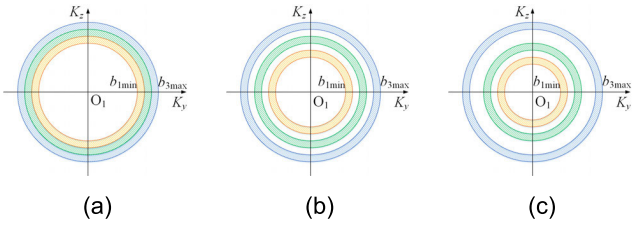

FIGURE 13. Typical spectrum distributions in $O_1K_yK_z$ plane (a) continuous spectrum distribution, (b) uniformly sparse spectrum distribution, (c) randomly sparse spectrum distribution.

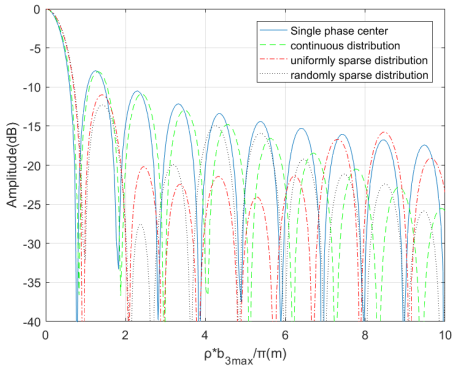

FIGURE 14. The point spread function of circular GBSAR with typical spectrum distributions.

TABLE 1. The 3D imaging performance of typical spectral distributions.

	Single-phase center	Multi-phase center		
Spectrum distribution	single	Continuous distribution	Uniformly sparse distribution	Randomly sparse distribution
PSLR (dB)	-7.9131	-8.0262	-10.9829	-12.2644
ISLR (dB)	-3.0077	-3.5164	-8.9582	-8.7124
Resolution (m)	2.6180	2.6180	2.9452	2.9452

continuous distribution, uniformly sparse distribution, and randomly sparse distribution is given in Table 1.

As can be seen from Table 1, compared with single-phase-center circular GBSAR, multi-phase-center circular GBSAR has lower sidelobes. Moreover, the sidelobe of sparse spectrum distribution are lower than that of continuous spectrum distribution. Meanwhile, the resolutions of these typical spectrum distributions in the $O_1Y'Z'$ plane have some difference, but they are almost close.

For multi-phase-center circular GBSAR with different spectrum distributions, the spectrum distribution is related to the phase center distribution. Here, we use $b_{1\max}/b_{3\max}$ and $b_{2\max}/b_{3\max}$ to represent the spectrum distribution. According to (15), the spectrum distribution can be expressed as

$$\begin{cases} b_{1\max}/b_{3\max} = \sin\beta_1/\sin\beta_3 \\ b_{2\max}/b_{3\max} = \sin\beta_2/\sin\beta_3 \end{cases} \tag{20}$$

Here, we use the ratio r_1/r_3 and the ratio r_2/r_3 to represent the phase center distribution. According to (18), the relationship between half-apex angle and phase center distribution is as follows

$$\begin{cases} \sin\beta_1 = r_1/R_1 \\ \sin\beta_2 = r_2/R_2 \\ \sin\beta_3 = r_3/R_3 \end{cases} \tag{21}$$

where, $r_1 r_2$ and r_3 are the rotating radius of phase centers a_1, a_2 and a_3, and r_3 is equal to the length of rotating arm L, R_1, R_2 and R_3 are the distance between the point target and phase centers.

According to (20) and (21), the relationship between the spectrum distribution and the phase center distribution can be expressed as

$$\begin{cases} r_1/r_3 = \left(b_{1\max}/b_{3\max}\right)\cdot\left(R_1/R_3\right) \\ r_2/r_3 = \left(b_{2\max}/b_{3\max}\right)\cdot\left(R_2/R_3\right) \end{cases} \tag{22}$$

When $L \ll x_c$, R_1, R_2 and R_3 are approximately the same. In the case of GBSAR, the length of the rotating arm L is much less than the point target's range. Thus, equation (22) can be simplified to

$$\begin{cases} r_1/r_3 \approx b_{1\max}/b_{3\max} \\ r_2/r_3 \approx b_{2\max}/b_{3\max} \end{cases} \tag{23}$$

According to the above analysis, we find that the multi-phase-center circular GBSAR with randomly sparse spectrum distribution has lower sidelobe. Moreover, the relationship between the spectrum distribution and the phase center distribution is given.

C. SIDELOBE ANALYSIS BASED ON PHASE CHANGE DIAGRAM

From the analysis in Section 4.2, it can be known that the sidelobe of multi-phase-center circular GBSAR in the $O_1Y'Z'$ plane is related to the spectrum distribution in the $O_1K_yK_z$ plane. In this section, under the condition of a given bandwidth-to-frequency ratio, an optimization method based on phase change diagram is used to get the optimal spectrum distribution for the lowest sidelobe. Here, phase change diagrams of multi-phase-center circular GBSAR with $N = 2$ and $N = 3$ are both given. Figure 15 gives the flow chart of the proposed sidelobe suppression method.

We set the peak sidelobe ratio of point spread function in (19) as the objective function, and its expression is as follows

$$PSLR = 20\log_{10}\left\{\max\left|\left[g_{mcyz}(\rho) - g_{main}(\rho)\right]/\mathrm{PP}_{\max}\right|\right\} \tag{24}$$

where, $\mathrm{PP}_{\max}$ is the main lobe peak and $g_{main}(\rho)$ is the main lobe portion of $g_{mcyz}(\rho)$, and its expression is

$$g_{main}(\rho) = g_{mcyz}(\rho)\cdot \mathrm{rect}\left(\rho/\rho_0\right) \tag{25}$$

where ρ_0 is the first zero crossing of $g_{mcyz}(\rho)$.

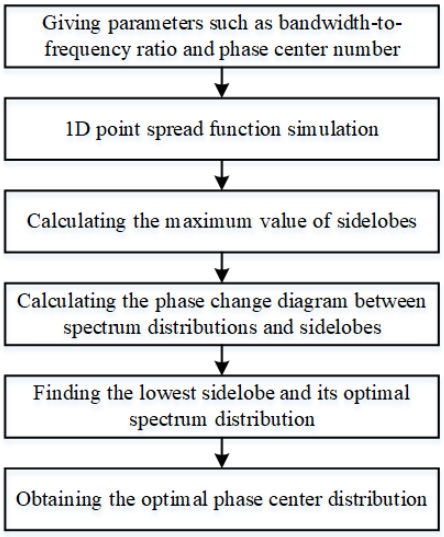

FIGURE 15. The flow chart of the proposed sidelobe suppression method.

In order to get the optimal spectrum distribution, we need to minimize the PSLR in (24). And the phase change curve can help us to find the minimum PSLR.

When the phase center number $N = 2$, phase change diagram is a 1-D curve. So, the value range of the spectrum distribution $b_{1\max}/b_{2\max}$ is (0,1). The PSLR curve with respect to spectrum distribution $b_{1\max}/b_{2\max}$ is shown in Figure 16.

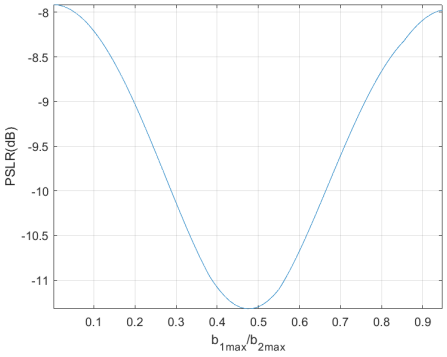

FIGURE 16. Phase change diagram ($N = 2$).

It can be seen from Figure 16 that there is an optimal spectrum distribution, which has the lowest PSLR. The optimal spectrum distribution is $b_{1\max}/b_{2\max} = 0.476$, $b_{2\max}/b_{2\max} = 1$, and its minimum PSLR is -11.32dB. According to the (23), its corresponding phase center distribution is $r_1 = 0.476L$, $r_2 = L$. Using this phase center distribution, the PSF shown in Figure 17 can be obtained, which has the best sidelobe characteristic under the conditions of $N = 2$ and $\alpha_a = 0.05$.

When the phase center number $N = 3$, phase change diagram is a 2-D figure. So, the value range of $b_{2\max}/b_{3\max}$ is (0,1) and the value range of $b_{1\max}/b_{3\max}$ is (0,1-$b_{2\max}/b_{3\max}$). The PSLR curve with respect to spectrum distribution $b_{1\max}/b_{3\max}$ and $b_{2\max}/b_{3\max}$ is shown in Figure 18. Where,

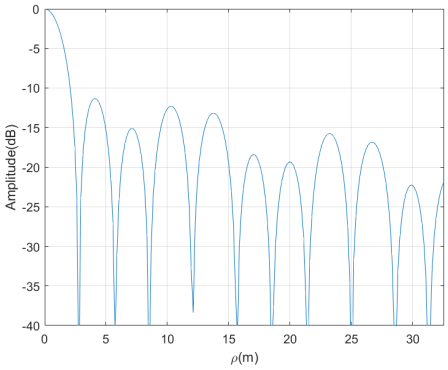

FIGURE 17. The point spread function of optimal phase center distribution ($N = 2$).

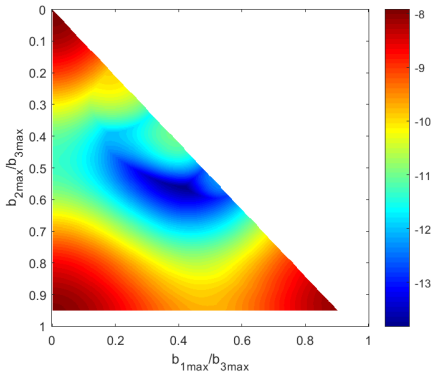

FIGURE 18. Phase change diagram ($N = 3$).

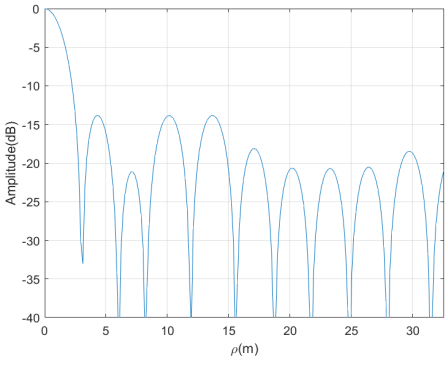

FIGURE 19. The point spread function of optimal phase center distribution ($N = 3$).

the grid interval dd = 0.002, the PSLR value is described by the color bar.

In Figure 18, the optimal spectrum distribution is $b_{1\max}/b_{3\max} = 0.42$, $b_{2\max}/b_{3\max} = 0.56$, $b_{3\max}/b_{3\max} = 1$, and its minimum PSLR is -13.83dB. According to (23), its corresponding phase center distribution is $r_1 = 0.42L$, $r_2 = 0.56L$, $r_3 = L$. The PSF shown in Figure 19 has the best sidelobe characteristic by using this phase center distribution.

The phase change diagram of the PSLR with respect to the spectrum distribution is given in this section. According to phase change diagram, the optimal spectrum distribution and the lowest PSLR can be found. The minimum PSLR in this example, for $N = 2$ and $N = 3$ are -11.32dB and -13.83dB, respectively, with the given condition of bandwidth-to-frequency ratio equal to 0.05. When the number of phase centers $N = 3$, the sidelobe suppression effect of the optimal spectrum distribution has already satisfied the needs for high-quality imaging. When $N = 2$, under the constraint of $\mathrm{b}_{1\max} < \alpha_a \cdot \mathrm{b}_{2\min}$, the actual calculation grid numbers is $0.95 \times (N_{dd} - 1)$, where N_{dd} is the grid numbers. Under the CPU configuration of Intel Core i7-8550U, the time consumption is 0.1283s. When $N = 3$, under the constraint of $\mathrm{b}_{1\max} < \alpha_a \cdot \mathrm{b}_{2\min}$ and $\mathrm{b}_{2\max} < \alpha_a \cdot \mathrm{b}_{3\min}$, the actual calculation grid numbers is $(0.45 \times N_{dd}^2 - 1.3 \times N_{dd} - 0.15)$. Under the same configuration, the time consumption is 22.9546s. It can be seen that the higher search space dimension, the more calculation complexity. If a lower PSLR is needed, the phase center number can be further increased, and the dimension of the phase change diagram is also increased. If the value of N is large, the dimension of the search space will become high. Thus, efficient searching method should be used to reduce the calculation complexity [29]–[31].

V. SPACE-VARIANT PROPERTY OF SIDELOBES

Space-variant property refers to the difference in point spread function (PSF) of targets at different positions.

According to the analysis in Section 3, multiple phase center influences the sidelobes of circular GBSAR, and it has little effect on its resolution. The resolution's space-variant property of circular GBSAR are consistent with that of traditional linear GBSAR. The resolution decreases with increasing range. The point spread function of circular GBSAR has the rotation property, which changes little with the azimuth. However, the resolution of different azimuths is still the same. Thus, we only need to concern about the space-variant property of sidelobes.

In this section, we will analyze whether the solved optimal spectrum distribution for sidelobe suppression works for the whole observation scene. Since the geometry of circular GBSAR is rotationally symmetric, we only need to analyze the sidelobe space-variance with respect to range and azimuth angle.

Firstly, we analyze the space-variance with respect to range. From the previous section, we know that the sidelobe is determined by the spectrum distribution. According to (20) to (23), it can be known that the spectrum distribution is related to $\sin\beta_n/\sin\beta_N$, and thus related to r_n/r_N. This means that for different ranges, the spectrum distribution will be slightly different, and the sidelobe will be slightly different too.

Figure 20 shows the geometry of targets at different ranges. Ranges from point targets P_1 and P_2 to point O are expressed as x_1 and x_2, respectively. Half-apex angles of points P_1 and P_2 are expressed as β_{1n} and β_{2n}. It can be seen from Figure 20, when the phase center distribution is given, the half-apex angle β_{mn} becomes smaller as the range x_m increases, so the sidelobe is related to the range x_m.

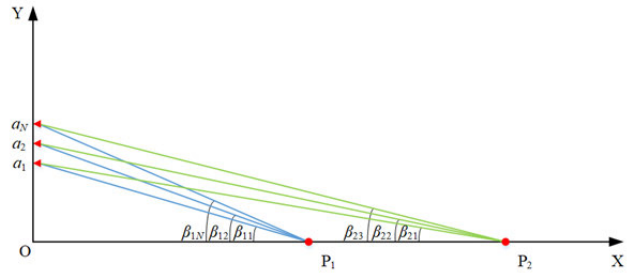

FIGURE 20. Geometry of phase centers and targets at different ranges.

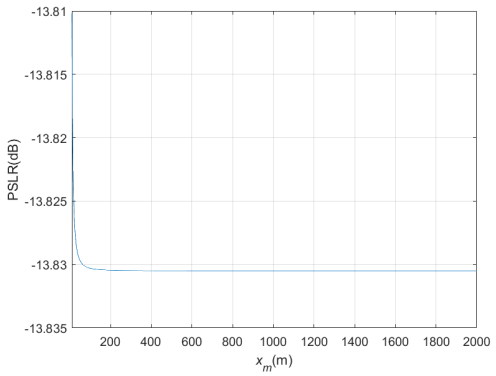

FIGURE 21. x_m- peak sidelobe ratio curve.

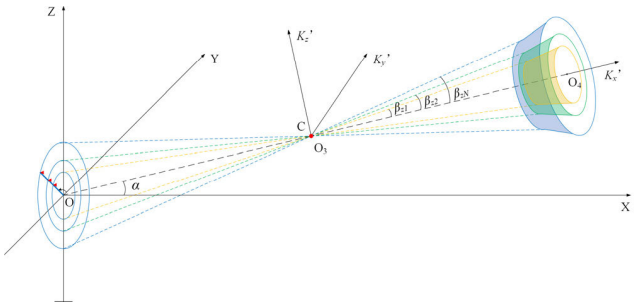

FIGURE 22. The 3D spectrum support of multi-phase-center circular GBSAR for the edge point target.

Figure 21 shows peak sidelobe ratio (PSLR) curve with respect to range, and the curve is obtained by numerical simulation. As can be seen from the figure, when range is above 20m, the sidelobe level is almost the same. This result is consistent with (23), that is when the rotating arm L is much less than the point target's range, the space-variance of sidelobe can be neglected.

Then, space-variance with respect to azimuth angle is analyzed. Figure 22 shows the 3D spectrum support of multi-phase-center circular GBSAR for the edge point target is a set of outer curved surfaces that approximate an elliptic truncated cone.

In Figure 22, α represents the azimuth angle of point targets, and $\alpha > 0$. Since α is rotationally symmetric with the X axis, the sidelobe variation with angle α is analyzed only in the XOZ plane. $\beta_{z1}, \beta_{z2}, \ldots, \beta_{zN}$ is the half-apex angle of elliptic truncated cone.

Figure 23 shows the 2D spectrum support of the edge point target in the $O_3K_y'K_z'$ plane. It can be known from Figure 23 that the spectrum support of edge point target in the $O_3K_y'K_z'$ plane is a set of elliptic rings. In Figure 23, $b_{n\min}$ and $c_{n\min}$ are the long axis and short axis of inner rings, $b_{n\max}$ and $c_{n\max}$ are the long axis and short axis of outer rings.

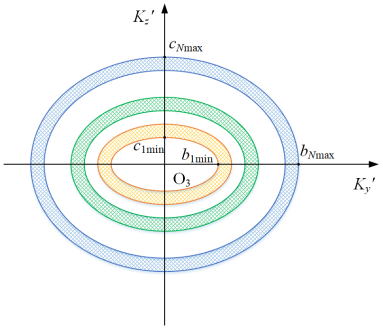

FIGURE 23. The 2D spectrum support of multi-phase-center circular GBSAR for the edge point target in $O_3K_y'K_z'$ plane.

According to (20), it can be known that the spectrum distribution is related to $\sin\beta_{yn}/\sin\beta_{yN}$ and $\sin\beta_{zn}/\sin\beta_{zN}$. Where, $\sin\beta_{yn}$ and $\sin\beta_{zn}$ are both related to the azimuth angle α. This means that for different azimuth angles, the spectrum distribution will be slightly different, and the sidelobe would be slightly different too.

Figure 24 shows PSLR curve with respect to azimuth angle, and the curve is obtained by numerical simulation. As can be seen from the figure, when azimuth angle is $0° \sim 15°$, the sidelobe level is almost the same. This result is consistent with (23), that is when the point target is within the beam irradiation range, the space-variance of sidelobe can be neglected.

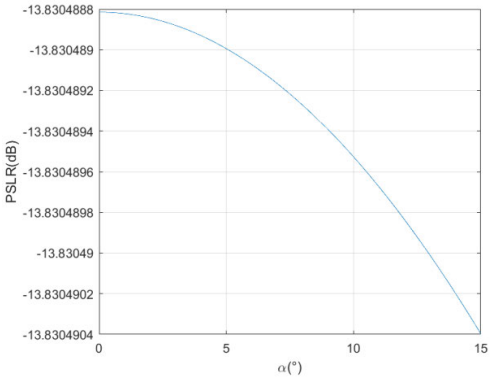

FIGURE 24. $\alpha-$ peak sidelobe ratio curve.

In order to verify the above analysis results, we respectively analyze the PSF of points A (50,0,0), B (506,0,0), and C (500,0,80). Where, points A and B are point targets on the X axis, points B and C are point targets with different azimuth angles. Points A, B, and C are all within the beam irradiation range.

Figure 25 shows the PSF of multi-phase-center circular GBSAR at points A and B by using optimal phase center

distribution. In the figure, their PSF are almost consistent, and their PSLR are both -13.83dB. Therefore, the space-variance with respect to range can be neglected.

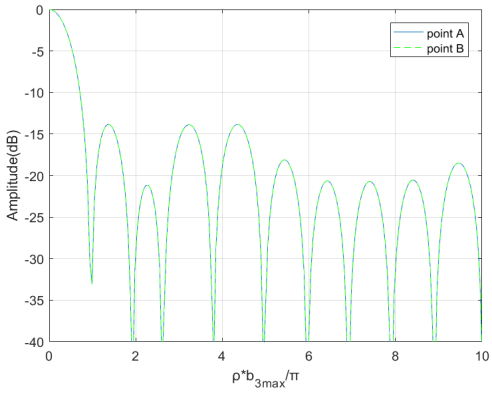

FIGURE 25. The point spread function of points A and B.

Figure 26 shows the PSF of multi-phase-center circular GBSAR at points B and C by using optimal phase center distribution. In the figure, their PSFs are almost consistent, and their PSLR are both -13.83dB. Therefore, the space-variance with respect to azimuth angle can be neglected.

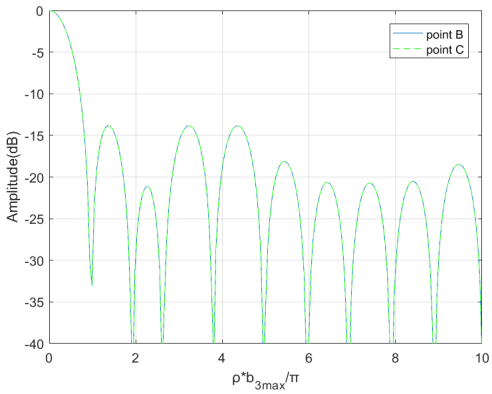

FIGURE 26. The point spread function of points B and C.

In summary, as the spatial position of point target changes, the sidelobe of multi-phase-center circular GBSAR slightly changes.

VI. SIMULATIONS

In this section, the effectiveness of the multi-phase-center sidelobe suppression method based on sparse spectrum optimal distribution is verified by point target's 3D imaging simulation. And we are going to compare the sidelobe of single-phase center, single-phase center with Hanning window, multi-phase centers with continuous spectrum distribution and multi-phase centers with sparse spectrum distribution.

Table 2 lists the simulation experiment parameters. GBSAR is usually used in slope monitoring. Its monitoring range is about 100m to 1000m, and its azimuth angle is about $-15°$ to $15°$. Thus, we set the distance of the point target to about 500m. The simulation parameters here are designed based on typical parameters of existing GBSAR systems. Its common center frequency is 17.5GHz and the bandwidth is often set to 1GHz. According to the existing NCUT-ArcSAR parameters, the rotating arm length L is set to 1m [32]. The phase center distribution r_{sn} is the parameter of circular GBSAR with optimal sparse spectrum distribution, and r_{cn} is the parameter of circular GBSAR with continuous spectrum distribution.

TABLE 2. Experiment parameters.

f_c (GHz)	α_a	L (m)	r_{sn} (m)	r_{cn} (m)
17.55	0.05	1	0.42, 0.56, 1	0.90, 0.95, 1

Here, the center frequency f_c is 17.55GHz and the bandwidth-to-frequency ratio α_a is 0.05, so the maximum frequency $f_{\max}$ is 18GHz and the bandwidth of the transmitted signal bandwidth B_r is 0.9GHz. The phase center distribution with continuous spectrum is expressed as r_{cn}, and the phase center distribution with sparse spectrum is expressed as r_{sn}. When $L = 1$m, the optimal phase center distribution is $r_1 = 0.42$, $r_2 = 0.56$, $r_3 = 1$, and the theoretical optimal peak sidelobe ratio (PSLR) is -13.83dB.

Under the condition of phase center number $N = 3$, the 3D imaging simulation results of the center point target for the single-phase center, single-phase center with Hanning window, multi-phase centers with continuous spectrum, and multi-phase centers with sparse spectrum are shown in Figure 27.

It can be seen from Figure 27(b) that the single-phase center with Hanning window method can't suppress the high sidelobes of circular GBSAR. Figure 27(c) shows that the sidelobe suppression effect of multi-phase-center circular GBSAR based on continuous spectrum distribution is very little. Figure 27(d) shows that the sidelobe of multi-phase-center circular GBSAR based on sparse spectrum is effectively suppressed.

In order to quantitatively analyze the imaging quality of these sidelobe suppression methods. Figure 28 shows their 2D slices in the YOZ plane.

Figure 28(b) shows that the sidelobes of single-phase center circular GBSAR after the Hanning window is higher than the original sidelobe. Figure 28(c) shows that the high sidelobes of multi-phase-center circular GBSAR based on continuous spectrum distribution is slightly suppressed. Figure 28(d) shows that the proposed method can obtain the significantly suppressed sidelobes. Thus, the proposed method has better sidelobe suppression effect than the existing methods.

Table 3 shows the imaging performance of simulation results for these sidelobe suppression methods in the YOZ plane. The simulation results in the YOZ plane is circular symmetric, so Table 3 only shows the peak sidelobe ratio

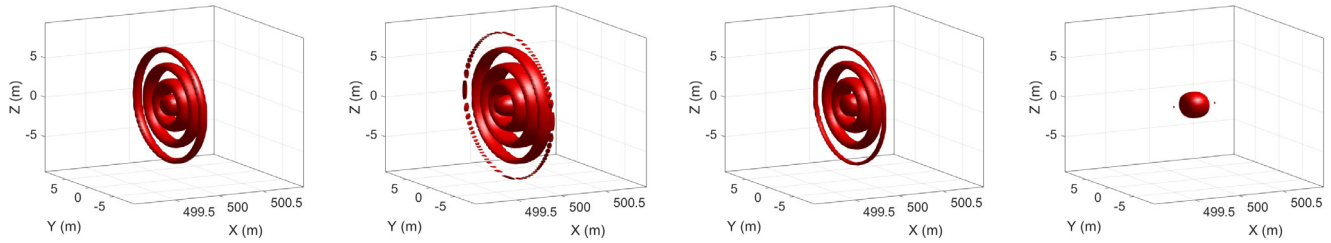

FIGURE 27. The 3D imaging simulation results of the center point target (a) Single-phase center, (b) Single-phase center with Hanning window, (c) Multi-phase centers with continuous spectrum distribution, (d) Multi-phase centers with sparse spectrum distribution.

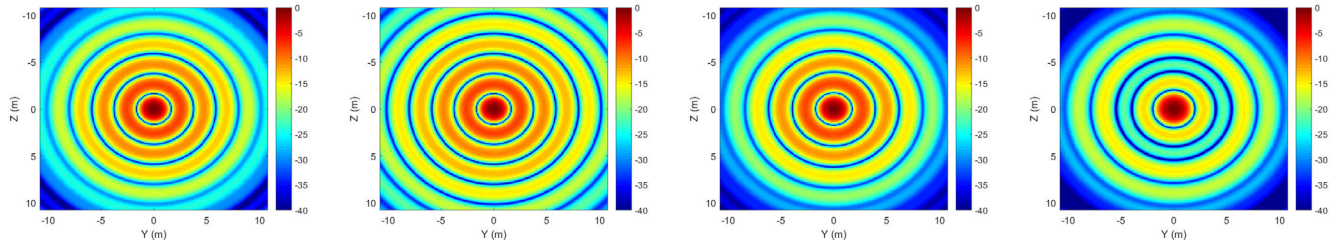

FIGURE 28. The 2D slices of the center point target in the YOZ plane (a) Single-phase center, (b) Single-phase center with Hanning window, (c) Multi-phase center with continuous spectrum distribution, (d) Multi-phase center with sparse spectrum distribution.

TABLE 3. Imaging performance comparison in the YOZ plane.

Distribution	Single-phase center	Single-phase center with Hanning window	Multi-phase centers with continuous spectrum	Multi-phase centers with sparse spectrum
PSLR (dB)	-7.9368	-7.9139	-8.0602	-13.8631
ISLR (dB)	-3.6660	-3.2672	-4.1489	-9.3079
Resolution (m)	1.7361	1.7361	1.7361	1.9531

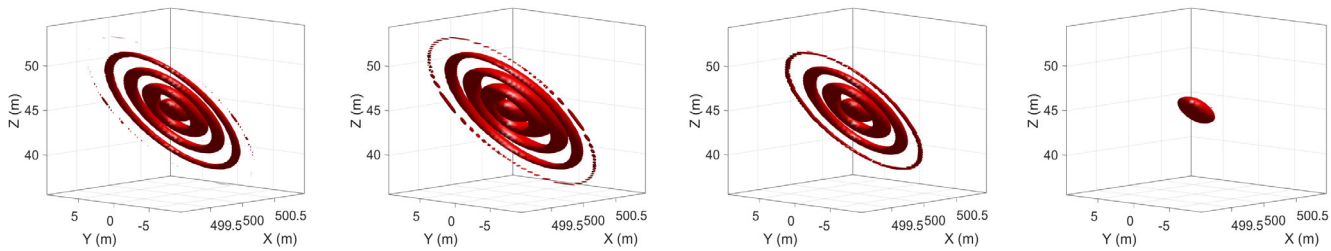

FIGURE 29. The 3D imaging simulation results of the edge point target (a) Single-phase center, (b) Single-phase center with Hanning window, (c) Multi-phase centers with continuous spectrum distribution, (d) Multi-phase centers with sparse spectrum distribution.

(PSLR), integral sidelobe ratio (ISLR) and resolution in the radial direction.

From results in Table 3, the sidelobe of multi-phase-center circular GBSAR is lower than that of single-phase-center circular GBSAR, it proves the sidelobe suppression capability of multi-phase-center circular GBSAR. Moreover, the sidelobe of the proposed method is significantly lower than that of the existing methods. Therefore, the sidelobe suppression capability of the proposed method is verified. Table 3 also shows that the resolution of the proposed method in the YOZ plane is slightly widened. However, it just has a little difference from that of the single-phase-center circular GBSAR.

In order to observe the 3D imaging performance of these sidelobe suppression methods in the edge point target. Figure 29 shows the 3D imaging simulation results of the edge point target.

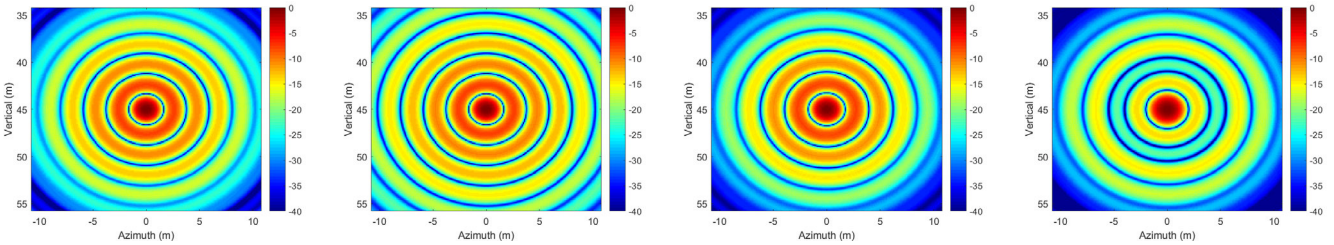

FIGURE 30. The 2D slices of the edge point target in the azimuth-vertical plane (a) Single-phase center, (b) Single-phase center with Hanning window, (c) Multi-phase center with continuous spectrum distribution, (d) Multi-phase center with sparse spectrum distribution.

TABLE 4. Imaging performance Comparison in the azimuth-vertical plane.

		Single-phase center	Single-phase center with Hanning window	Multi-phase centers with continuous spectrum	Multi-phase centers with sparse spectrum
Azimuth	PSLR (dB)	-7.8916	-7.9154	-8.0152	-13.8396
	ISLR (dB)	-3.6168	-3.2764	-4.0968	-9.2914
	Resolution (m)	1.7361	1.7361	1.7361	1.9531
Vertical	PSLR (dB)	-8.0049	-7.9154	-8.1328	-14.0026
	ISLR (dB)	-3.7014	-3.2764	-4.1845	-9.3487
	Resolution (m)	1.7431	1.7431	1.7431	1.9610

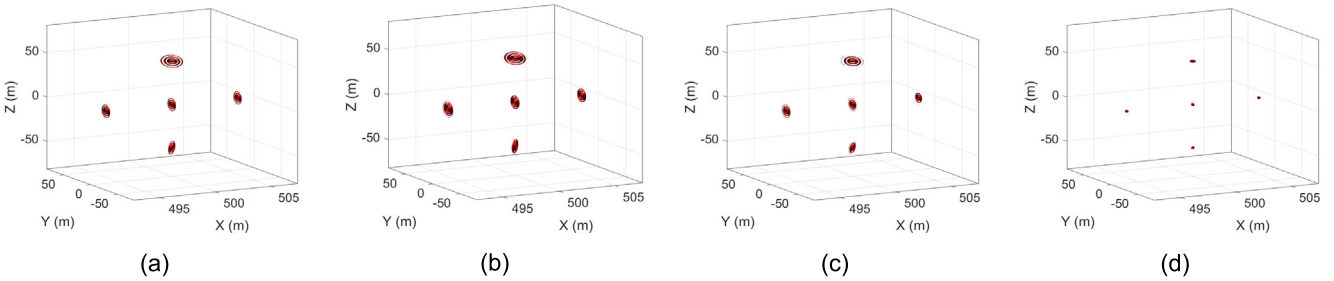

FIGURE 31. The 3D imaging simulation results of lattice targets (a) Single-phase center, (b) Single-phase center with Hanning window, (c) Multi-phase centers with continuous spectrum distribution, (d) Multi-phase centers with sparse spectrum distribution.

Figure 30 shows that the 2D slices of the edge point target in the azimuth-vertical plane is similar to those of the center point target in the YOZ plane.

In order to analyze the imaging performance of simulation results in the azimuth-vertical plane. Table 4 shows the peak sidelobe ratio (PSLR), integral sidelobe ratio (ISLR) and resolution in the azimuth direction and in the vertical direction.

From results in Table 4, the azimuth imaging performance is different from the vertical imaging performance, but they are quite similar. In addition, the imaging performance of these sidelobe suppression methods at the edge point target is closed to that of the sidelobe suppression methods at the center point target. Thus, it is proved that the proposed method is effective at the edge point target.

In order to compare the 3D imaging performance of these sidelobe suppression methods in the whole monitoring scenario. The 3D imaging simulation results of lattice targets is shown in Figure 31.

Figure 31 shows that the proposed method has lower sidelobes than the existing methods for lattice targets. Hence, the proposed method is applicable to the whole monitoring scenario.

VII. CONCLUSION

In this paper, a new multi-phase-center sidelobe suppression method for circular GBSAR based on sparse spectrum is proposed. This method can effectively suppress the sidelobes in the plane perpendicular to range with limited phase centers. Multi-phase-center circular GBSAR provides extra spectrum information to the originally unknown region inside the ring-shaped spectrum. Thus, the sidelobe of multi-phase-center circular GBSAR is lower than single-phase-center circular GBSAR. By comparing point spread function of

typical spectrum distributions, we find that multi-phase-center with different spectrum distributions have different effects on sidelobe suppression. Under the condition of given phase center number, the optimal spectrum distribution is obtained with the phase change diagram. In the example of this paper, the sidelobe can be reduced from −7.9dB to −13.8dB with three phase centers. The suppressed sidelobe level is acceptable for GBSAR. The space-variant property is also discussed, and since, the rotating arm is far less than the target range in GBSAR applications, the space-variance of sidelobes can be neglected. Thereby, the obtained optimal phase center distribution applies to the whole observation scene. Moreover, the simulation evaluates the 3D imaging performance of multi-phase-center circular GBSAR. Simulation results also show that the optimal spectrum distribution obtained by the proposed method has better sidelobe characteristic.

REFERENCES

[1] M. Pieraccini, N. Casagli, G. Luzi, D. Tarchi, D. Mecatti, L. Noferini, and C. Atzeni, "Landslide monitoring by ground-based radar interferometry: A field test in Valdarno (Italy)," *Int. J. Remote Sens.*, vol. 24, no. 6, pp. 1385–1391, Jan. 2003.

[2] W. Frodella, T. Salvatici, V. Pazzi, S. Morelli, and R. Fanti, "GB-InSAR monitoring of slope deformations in a mountainous area affected by debris flow events," *Natural Hazards Earth Syst. Sci.*, vol. 17, no. 10, pp. 1779–1793, Oct. 2017.

[3] F. Di Traglia, T. Nolesini, E. Intrieri, F. Mugnai, D. Leva, M. Rosi, and N. Casagli, "Review of ten years of volcano deformations recorded by the ground-based InSAR monitoring system at Stromboli volcano: A tool to mitigate volcano flank dynamics and intense volcanic activity," *Earth-Sci. Rev.*, vol. 139, pp. 317–335, Dec. 2014.

[4] S. Kuraoka, Y. Nakashima, R. Doke, and K. Mannen, "Monitoring ground deformation of eruption center by ground-based interferometric synthetic aperture radar (GB-InSAR): A case study during the 2015 phreatic eruption of Hakone volcano," *Earth, Planets Space*, vol. 70, no. 1, pp. 181–189, Dec. 2018.

[5] L. Noferini, D. Mecatti, G. Macaluso, M. Pieraccini, and C. Atzeni, "Monitoring of belvedere glacier using a wide angle GB-SAR interferometer," *J. Appl. Geophys.*, vol. 68, no. 2, pp. 289–293, Jun. 2009.

[6] N. Dematteis, G. Luzi, D. Giordan, F. Zucca, and P. Allasia, "Monitoring alpine glacier surface deformations with GB-SAR," *Remote Sens. Lett.*, vol. 8, no. 10, pp. 947–956, Oct. 2017.

[7] C. Huang, H. Xia, and J. Hu, "Surface deformation monitoring in coal mine area based on PSI," *IEEE Access*, vol. 7, pp. 29672–29678, 2019.

[8] Y. Luo, H. Song, R. Wang, Y. Deng, F. Zhao, and Z. Xu, "Arc FMCW SAR and applications in ground monitoring," *IEEE Trans. Geosci. Remote Sens.*, vol. 52, no. 9, pp. 5989–5998, Sep. 2014.

[9] M. Pieraccini, M. Fratini, F. Parrini, and C. Atzeni, "Dynamic monitoring of bridges using a high-speed coherent radar," *IEEE Trans. Geosci. Remote Sens.*, vol. 44, no. 11, pp. 3284–3288, Nov. 2006.

[10] M. Pieraccini and L. Miccinesi, "An interferometric MIMO radar for bridge monitoring," *IEEE Geosci. Remote Sens. Lett.*, vol. 16, no. 9, pp. 1383–1387, Sep. 2019.

[11] F. Pratesi, T. Nolesini, S. Bianchini, D. Leva, L. Lombardi, R. Fanti, and N. Casagli, "Early warning GBInSAR-based method for monitoring volterra (Tuscany, Italy) city walls," *IEEE J. Sel. Topics Appl. Earth Observ. Remote Sens.*, vol. 8, no. 4, pp. 1753–1762, Apr. 2015.

[12] M. Alberto, F. Coppi, A. Bicci, and G. Alli, "SPARX, a MIMO array for ground-based radar interferometry," *Sensors*, vol. 19, no. 2, pp. 252–262, 2019.

[13] Y. Ji, H. Han, and H. Lee, "Construction and application of tomographic SAR system based on GB-SAR system," in *Proc. IEEE Geosci. Remote Sens. Symp.*, Quebec City, QC, Canada, Jul. 2014, pp. 1891–1894.

[14] M. Pieraccini, N. Rojhani, and L. Miccinesi, "Ground based synthetic aperture radar with 3D imaging capability," in *Proc. 15th Eur. Radar Conf. (EuRAD)*, Madrid, Spain, Sep. 2018, pp. 206–209.

[15] T. G. Yitayew, L. Ferro-Famil, T. Eltoft, and S. Tebaldini, "Tomographic imaging of fjord ice using a very high resolution ground-based SAR system," *IEEE Trans. Geosci. Remote Sens.*, vol. 55, no. 2, pp. 698–714, Feb. 2017.

[16] M. Pieraccini, N. Agostini, F. Papi, and S. Rocchio, "A rotating antenna ground-based SAR," in *Proc. Eur. Radar Conf. (EuRAD)*, Paris, France, Sep. 2015, pp. 493–496.

[17] M. Pieraccini and L. Miccinesi, "RotoSAR for monitoring bridges," in *Proc. 14th EuRAD*, Nuremberg, Germany, Oct. 2017, pp. 311–314.

[18] M. Pieraccini, F. Papi, and S. Rocchio, "SAR imagery by RotoSAR," in *Proc. IEEE Int. Conf. Microw., Commun., Antennas Electron. Syst. (COMCAS)*, Tel Aviv, Israel, Nov. 2015, pp. 1–5.

[19] S. R. DeGraaf, "Sidelobe reduction via adaptive FIR filtering in SAR imagery," *IEEE Trans. Image Process.*, vol. 3, no. 3, pp. 292–301, May 1994.

[20] C. Li, Z. Yu, and J. Chen, "Overview of techniques for improving high-resolution spaceborne SAR imaging and image quality," *J. Radars*, vol. 8, no. 6, pp. 717–731, 2019.

[21] B. H. Smith, "Generalization of spatially variant apodization to noninteger Nyquist sampling rates," *IEEE Trans. Image Process.*, vol. 9, no. 6, pp. 1088–1093, Jun. 2000.

[22] H. Li, X. He, D. Tao, Y. Tang, and R. Wang, "Joint medical image fusion, denoising and enhancement via discriminative low-rank sparse dictionaries learning," *Pattern Recognit.*, vol. 79, pp. 130–146, Jul. 2018.

[23] Y. Liu, X. Chen, R. K. Ward, and Z. J. Wang, "Medical image fusion via convolutional sparsity based morphological component analysis," *IEEE Signal Process. Lett.*, vol. 26, no. 3, pp. 485–489, Mar. 2019.

[24] Z. Zhu, M. Zheng, G. Qi, D. Wang, and Y. Xiang, "A phase congruency and local Laplacian energy based multi-modality medical image fusion method in NSCT domain," *IEEE Access*, vol. 7, pp. 20811–20824, 2019.

[25] J. Ming, X. Zhang, L. Pu, and J. Shi, "PSF analysis and ground test results of a novel circular array 3-D SAR system," *J. Radars*, vol. 7, no. 6, pp. 770–776, 2018.

[26] G. Wang, F. Qi, Z. Liu, C. Liu, C. Xing, and W. Ning, "Comparison between back projection algorithm and range migration algorithm in terahertz imaging," *IEEE Access*, vol. 8, pp. 18772–18777, 2020.

[27] L. Chen, D. An, and X. Huang, "A backprojection-based imaging for circular synthetic aperture radar," *IEEE J. Sel. Topics Appl. Earth Observ. Remote Sens.*, vol. 10, no. 8, pp. 3547–3555, Aug. 2017.

[28] M. Soumekh, *Synthetic Aperture Radar Signal Processing With MATLAB Algorithms*. New York, NY, USA: Hoboken, NJ, USA: Wiley, 1999, pp. 486–552.

[29] T. S. J. Laseetha and A. R. Sukanesh, "Synthesis of linear antenna array using genetic algorithm to maximize sidelobe level reduction," *Int. J. Comput. Appl.*, vol. 20, no. 7, pp. 27–33, Apr. 2011.

[30] H. Li, Y. Jiang, Y. Ding, J. Tan, and J. Zhou, "Low-sidelobe pattern synthesis for sparse conformal arrays based on PSO-SOCP optimization," *IEEE Access*, vol. 6, pp. 77429–77439, 2018.

[31] X. Xu, C. Liao, L. Zhou, and F. Peng, "Grating lobe suppression of non-uniform arrays based on position gradient and sigmoid function," *IEEE Access*, vol. 7, pp. 106407–106416, 2019.

[32] Y. Wang, W. Hong, Y. Zhang, Y. Lin, Y. Li, Z. Bai, Q. Zhang, S. Lv, H. Liu, and Y. Song, "Ground-based differential interferometry SAR: A review," *IEEE Geosci. Remote Sens. Mag.*, vol. 8, no. 1, pp. 43–70, Mar. 2020.

YANPING WANG (Associate Member, IEEE) received the Ph.D. degree from the Institute of Electronics, Chinese Academy of Sciences, Beijing, China, in 2003. He has been the Deputy Director of the National Key Laboratory of Microwave Imaging Technology, Chinese Academy of Sciences. He is currently with the School of Information Science and Technology, North China University of Technology, Beijing. His research directions are intelligent radar, radar deformation monitoring, and intelligent early warning technology. He is a member of the IET international radar conference procedure committee.

QIMING ZHANG received the B.S. degree in electronic information engineering from Jilin University, in 2018. He is currently pursuing the master's degree with the School of Information Science and Technology, North China University of Technology, Beijing, China. His research interest includes synthetic aperture radar imaging.

YUN LIN received the Ph.D. degree from the Institute of Electronics, Chinese Academy of Sciences, in 2011. From 2012 to 2018, she was with the Institute of Electronics, Chinese Academy of Sciences, as a Scientist. She is currently an Associate Professor with School of Electronic Information Engineering, North China University of Technology, Beijing, China. Her current interests include circular SAR imaging and anisotropic scattering target detection.

ZIHENG ZHAO received the B.S. degree in electronic information engineering from the North China University of Technology, Beijing, China, in 2019. He is currently pursuing the master's degree with the School of Electronics and Communication Technology, North China University of Technology. His research interest includes synthetic aperture radar imaging.

YANG LI received the Ph.D. degree from the Institute of Electronics, Chinese Academy of Sciences. He is currently with the School of Information Science and Technology, North China University of Technology, Beijing, China. His research directions are intelligent radar, radar deformation monitoring, and intelligent early warning technology.